The dielectric function in p-type III–V semiconductors

G Irmer, J Monecke and M Wenzel

Institute of Theoretical Physics, University of Mining and Technology, D-09596 Freiberg, Germany

Abstract. The dependences on frequency, wavevector, temperature, and carrier damping of the dielectric functions of p-type semiconductors with zinc-blende or diamond structure are calculated. Analytic expressions are derived in the random-phase approximation, and finite-lifetime effects are included in a relaxation time approximation. The ranges of dominant intraband and interband transitions are discussed for the example of GaAs. Interband transitions are very significant at low temperatures and small wavevectors. The theoretical results are compared with light scattering experiments on p-GaAs.

1. Introduction

In zinc-blende-type (e.g. GaAs, InP, etc) as well as in diamond-type semiconductors (Ge, Si) the top of the valence band, located at $k = 0$, is fourfold degenerate and splits for $k \neq 0$ into the two bands of heavy and light holes, each doubly degenerate [7–10]. The low-frequency dielectric function which describes the response of the free holes to electromagnetic fields depends on the intraband and interband transitions. Combescot and Nozières [1] have shown that the interband transitions between the bands of heavy and light holes can influence the dielectric constant remarkably in degenerate p-type Ge-like semiconductors. Their calculations were performed in the limits $q = 0$ and $T = 0$, and extended in a later paper [2] to $q \neq 0$ in terms of a power series expansion to lowest order in q. Bardyszewski [3] included the full q-dependence in the limit $T = 0$ K. The free-hole mobility is often small in comparison with the free-electron mobility in n-type semiconductors. Therefore, carrier damping effects should be considered, too. Finite-lifetime effects in a relaxation time approximation were included for the intraband and interband transitions by Monecke [4]. In his work, analytic expressions for the dielectric function and the conductivity are given in the limits $q = 0$ and $T = 0$.

   The purpose of this paper is to extend earlier calculations of the dielectric function in p-type semiconductors with tetrahedrally bonded atoms, including finite temperatures, the wavevector dependence, and lifetime effects, and to compare the results with those of light scattering experiments on p-GaAs.

2. The dielectric function in the relaxation time approximation

A particle-number-conserving relaxation time approximation for the dielectric function of p-type semiconductors was derived in [4]. In the present paper these expressions are generalized, including the effects of finite temperatures and wavevectors.

The low-frequency optical and electrical properties of p-type semiconductors with diamond and zinc-blende structure are determined by intraband transitions of the free holes within the bands of the heavy holes (index 1) and light holes (index 2), and by interband transitions between the bands (indices 12 and 21). The response of the free carriers to an electromagnetic field is given by the dielectric function

$$\varepsilon = \varepsilon_\infty + \sum_{\upsilon,\upsilon'=1}^{2} \chi^{\upsilon\upsilon'}(\boldsymbol{q},\omega) = \varepsilon_\infty + \varepsilon_{intra} + \varepsilon_{inter} \tag{1}$$

with

$$\chi^{\upsilon\upsilon} = \tilde{\chi}^{\upsilon\upsilon}(\boldsymbol{q},\omega+\mathrm{i}\Gamma_\upsilon)\left(1 - \frac{\mathrm{i}\Gamma_\upsilon}{\omega+\mathrm{i}\Gamma_\upsilon}\left[1 - \frac{\tilde{\chi}^{\upsilon\upsilon}(\boldsymbol{q},\omega+\mathrm{i}\Gamma_\upsilon)}{\tilde{\chi}^{\upsilon\upsilon}(\boldsymbol{q},0)}\right]\right)^{-1} \tag{2}$$

where $\upsilon = \upsilon'$ and $\Gamma_\upsilon = \Gamma_{\upsilon\upsilon}$, and

$$\chi^{\upsilon\upsilon'} = \tilde{\chi}^{\upsilon\upsilon'}(\boldsymbol{q},\omega+\mathrm{i}\Gamma_{12})\left(1 - \frac{\mathrm{i}\Gamma_{12}}{\omega+\mathrm{i}\Gamma_{12}}\left[1 - \frac{\tilde{\chi}^{12}(\boldsymbol{q},\omega+\mathrm{i}\Gamma_{12}) + \tilde{\chi}^{21}(\boldsymbol{q},\omega+\mathrm{i}\Gamma_{12})}{\tilde{\chi}^{12}(\boldsymbol{q},0) + \tilde{\chi}^{21}(\boldsymbol{q},0)}\right]\right)^{-1} \tag{3}$$

where $\upsilon \neq \upsilon'$ and $\Gamma_{12} = \Gamma_{21}$, with

$$\tilde{\chi}^{\upsilon\upsilon'}(\boldsymbol{q},\omega+\mathrm{i}\Gamma_{\upsilon\upsilon'}) = \frac{e^2}{\varepsilon_0 q^2} \sum_k \frac{f_{\upsilon'}(\boldsymbol{k}+\boldsymbol{q}/2) - f_\upsilon(\boldsymbol{k}-\boldsymbol{q}/2)}{\hbar\omega + \mathrm{i}\hbar\Gamma_{\upsilon\upsilon'} - [\varepsilon_{\upsilon'}(\boldsymbol{k}+\boldsymbol{q}/2) - \varepsilon_\upsilon(\boldsymbol{k}-\boldsymbol{q}/2)]} G_{\upsilon\upsilon'} \tag{4}$$

where

$$G_{\upsilon\upsilon'} = |\langle \boldsymbol{k}-\boldsymbol{q}/2, \upsilon|e^{-\mathrm{i}\boldsymbol{q}\cdot\boldsymbol{r}}|\boldsymbol{k}+\boldsymbol{q}/2, \upsilon'\rangle|^2. \tag{5}$$

Equations (2) and (3) take into account the local particle-number conservation in the case of finite-lifetime effects [5, 4], $\Gamma \sim 1/\tau$ being the appropriate damping constants, f_υ the Fermi distribution function, and $\boldsymbol{q}$ the transferred wavevector. The equal-energy surfaces ε_υ in equation (4) are warped [8]; the approximation of the two subbands by spherical and parabolic energy dispersion relationships [9] gives $\varepsilon_\upsilon = \hbar^2 k^2/2m_\upsilon$. We approximate the overlap integrals between the periodic parts of the Bloch functions at the Γ point in equation (5) by

$$G_{11} = G_{22} = \frac{1}{4}(1 + 3\cos^2\Theta) \tag{6}$$

$$G_{12} = G_{21} = \frac{3}{4}\sin^2\Theta \tag{7}$$

where Θ is the angle between the vectors $\boldsymbol{k}-\boldsymbol{q}/2$ and $\boldsymbol{k}+\boldsymbol{q}/2$. These expressions are widely used in investigations of valence band properties [6].

Replacing the sum in equation (4) by integrals over the $\boldsymbol{k}$-space, some integrations can be carried out analytically, and we arrive at the following expressions for the intraband part:

$$\begin{aligned}
\tilde{\chi}^{\upsilon\upsilon} = c_1 y^{-3/2} \int_{x=0}^{\infty} f(x)\,\mathrm{d}x \Bigg\{ &\ln\frac{(y+\tilde{\Omega}+2\sqrt{xy})\,(y-\tilde{\Omega}+2\sqrt{xy})}{(y+\tilde{\Omega}-2\sqrt{xy})\,(y-\tilde{\Omega}-2\sqrt{xy})} \\
&+ \frac{3}{2}\sqrt{\frac{y}{x}} - \frac{3}{4}\frac{(x-y)^2}{(x^2-\tilde{\Omega}^2)}\ln\left|\frac{\sqrt{x}+\sqrt{y}}{\sqrt{x}-\sqrt{y}}\right| \\
&+ \frac{3}{16}\frac{[(y+\tilde{\Omega})^2-4xy]}{(x-\tilde{\Omega})}\ln\frac{y+\tilde{\Omega}+2\sqrt{xy}}{y+\tilde{\Omega}-2\sqrt{xy}} \\
&+ \frac{3}{16}\frac{[(y-\tilde{\Omega})^2-4xy]}{(x+\tilde{\Omega})}\ln\frac{y-\tilde{\Omega}+2\sqrt{xy}}{y-\tilde{\Omega}-2\sqrt{xy}} \Bigg\}
\end{aligned} \tag{8}$$

and for the interband part

$$
\begin{aligned}
\tilde{\chi}^{v'v} = \frac{c_1}{y^{3/2}} \int_{x=0}^{\infty} dx \Bigg\{ &-\frac{3}{4}\sqrt{\frac{y}{x}} \left[\rho f_v(x) + f_{v'}(x) \right] \\
&+ \frac{3(x-y)^2}{8x} \left[\frac{f_v(x)}{(x-\tilde{\Omega})} + \frac{f_{v'}(x)}{(x/\rho + \tilde{\Omega})} \right] \ln\left| \frac{\sqrt{x}+\sqrt{y}}{\sqrt{x}-\sqrt{y}} \right| \\
&- \frac{3 f_v(x)\left[(y + \rho\tilde{\Omega} - (\rho-1)x)^2 - 4xy \right]}{16x(x-\tilde{\Omega})} \\
&\times \ln\frac{y + \rho\tilde{\Omega} - (\rho-1)x + 2\sqrt{xy}}{y + \rho\tilde{\Omega} - (\rho-1)x - 2\sqrt{xy}} \\
&- \frac{3 f_{v'}(x)\left[(y - \tilde{\Omega} + (\rho-1)x/\rho)^2 - 4xy \right]}{16x(x/\rho + \tilde{\Omega})} \\
&\times \ln\frac{y - \tilde{\Omega} + (\rho-1)x/\rho + 2\sqrt{xy}}{y - \tilde{\Omega} + (\rho-1)x/\rho - 2\sqrt{xy}} \Bigg\}.
\end{aligned}
\tag{9}
$$

In equations (8) and (9) the following abbreviations were used:

$$
c_1 = \frac{e^2 \sqrt{m_v}}{4\pi^2 \varepsilon_0 \hbar \sqrt{2k_B T}}
\tag{10}
$$

$$
x = \frac{\varepsilon_v}{k_B T} = \frac{\hbar^2 k^2}{2m_v k_B T}
\tag{11}
$$

$$
y = \frac{\hbar^2 q^2}{2m_v k_B T}
\tag{12}
$$

$$
\tilde{\Omega} = \frac{\hbar\tilde{\omega}}{k_B T}
\tag{13}
$$

$$
\tilde{\omega} = \omega + i\Gamma_{vv'}
\tag{14}
$$

$$
\rho = \frac{m_{v'}}{m_v}
\tag{15}
$$

$$
f_v(x) = \left(1 + \exp\left(x + \frac{E_v - \xi}{k_B T} \right) \right)^{-1}
\tag{16}
$$

$$
f_{v'}(x) = \left(1 + \exp\left(x/\rho + \frac{E_v - \xi}{k_B T} \right) \right)^{-1}.
\tag{17}
$$

m_v is the effective mass of hole type v, E_v the energy of the valence band edge, and ξ is the chemical potential.

The behaviour of the dielectric function for small wavevectors is often of interest. We prove in the following that the equations (8) and (9) lead to the well known $q \to 0$ limits: the overlap integrals in equation (6) are then $G_{11} = G_{22} \approx 1$, and the intraband part (8) reduces to

$$
\tilde{\chi}^{vv} = c_1 y^{-3/2} \int_{x=0}^{\infty} f(x)\, dx \left\{ \ln\frac{(y + \tilde{\Omega} + 2\sqrt{xy})(y + \tilde{\Omega} - 2\sqrt{xy})}{(y + \tilde{\Omega} - 2\sqrt{xy})(y - \tilde{\Omega} - 2\sqrt{xy})} \right\}
\tag{18}
$$

which coincides with the corresponding expression of the Lindhard function for electrons.

Expanding the expression in the braces up to the fourth order in $\sqrt{y/x}$, we get

$$\tilde{\chi}^{\upsilon\upsilon} = c_1 \int_{x=0}^{\infty} f(x) \, dx \left\{ -\frac{8\sqrt{x}}{\tilde{\Omega}^2} - \frac{y(1 + 8x^2/\tilde{\Omega}^2)}{2\sqrt{x}(x^2 - \tilde{\Omega}^2)} \right\} \approx -\frac{8c_1}{\tilde{\Omega}^2} \int_{x=0}^{\infty} f(x)\sqrt{x} \, dx$$

$$= -\frac{8c_1}{\tilde{\Omega}^2} F_{1/2}\left(\frac{E_V - \xi}{k_B T} \right). \tag{19}$$

The dependence of the free-hole concentration p_υ on the Fermi integral $F_{1/2}$ is

$$p_\upsilon = p_{0\upsilon} \frac{2}{\sqrt{\pi}} F_{1/2}\left(\frac{E_V - \xi}{k_B T} \right) \tag{20}$$

with

$$p_{0\upsilon} = \frac{2}{h^3} (2\pi m_\upsilon k_B T)^{3/2}. \tag{21}$$

Therefore, we obtain

$$\tilde{\chi}^{\upsilon\upsilon} = -\frac{e^2 p_\upsilon}{\varepsilon_0 m_\upsilon \tilde{\omega}^2} = -\frac{\varepsilon_\infty \omega_{p\upsilon}^2}{(\omega + i\Gamma_\upsilon)^2}. \tag{22}$$

Introducing $\tilde{\chi}^{\upsilon\upsilon}$ in equation (2), with $\tilde{\chi}^{\upsilon\upsilon}(0,0) \to \infty$, it follows that the intraband part is given by the Drude expression

$$\chi^{\upsilon\upsilon} = -\frac{\varepsilon_\infty \omega_{p\upsilon}^2}{\omega(\omega + i\Gamma_\upsilon)} \qquad (\upsilon = \upsilon') \tag{23}$$

$\omega_{p\upsilon}$ is the plasma frequency of the heavy ($\upsilon = 1$) and light ($\upsilon = 2$) holes:

$$\omega_{p\upsilon} = \sqrt{\frac{e^2 p_\upsilon}{\varepsilon_0 \varepsilon_\infty m_\upsilon}}. \tag{24}$$

In the case of the interband contributions, the expansion of the formula in the braces in equation (9) in powers of $\sqrt{y/x}$ gives for small wavevectors

$$\tilde{\chi}^{\upsilon'\upsilon}(\tilde{\omega}, 0) \approx 2c_1 \int_{x=0}^{\infty} \frac{dx}{\sqrt{x}} \frac{f_\upsilon(x) - f_{\upsilon'}(x)}{\tilde{\Omega} - x + x/\rho}$$

$$= \frac{e^2}{2\pi^2 \varepsilon_0} \int_{k=0}^{\infty} dk \frac{f_\upsilon(k) - f_{\upsilon'}(k)}{\hbar\omega + i\hbar\Gamma_{\upsilon'\upsilon} - [\varepsilon_\upsilon(k) - \varepsilon_{\upsilon'}(k)]}$$

$$= \tilde{\chi}^{\bar{\upsilon}\upsilon'}(-\tilde{\omega}, 0). \tag{25}$$

3. Discussion

The following examples are based on parameters characteristic of GaAs: $m_1 = 0.56 m_e$, $m_2 = 0.08 m_e$, $\rho = m_2/m_1 = 0.14$, $\varepsilon_\infty = 10.9$. The assumed free-carrier concentration is $p = 10^{18}$ cm^{-3}. These values set the Fermi energy in the degenerate case to $E_F = 6.3$ meV, and the values of the Fermi vectors to $k_{F1} = 3 \times 10^6$ cm^{-1} and $k_{F2} = 1.1 \times 10^6$ cm^{-1}.

Before considering the dielectric function in more general cases with more relevance to the properties of the p-type semiconductors and the experimental conditions, we first discuss the well known [1] limiting case of wavevector $q \to 0$ and small relaxation times $\Gamma_1 = \Gamma_2 = \Gamma_{12} \ll \hbar\omega$.
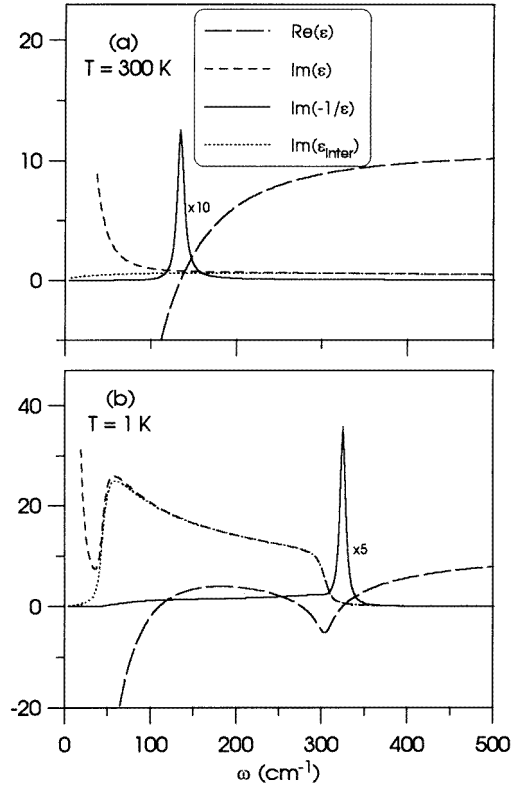
Figure 1. The dielectric function $\varepsilon(\omega)$ for small wavevectors and small carrier dampings at (a) room temperature ($\hbar\omega \lesssim kT$) and (b) low temperature ($\hbar\omega \gg kT$). The parameters used are: $q = 0$, $\Gamma_1 = \Gamma_2 = \Gamma_{12} = 1$ cm^{-1}.

3.1. Wavevector $q \to 0$, small relaxation times

3.1.1. *Room temperature, $\hbar\omega \lesssim kT$.* The numerical calculations were performed for $T = 300$ K. As can be seen in figure 1(a), the influence of the interband part is negligible, because the interband transitions are spread out over a broad energy range. The intraband part dominates, and equation (1) can be simplified to the Drude expression

$$\varepsilon = \varepsilon_\infty \left(1 - \frac{\omega_{p1}^2}{\omega(\omega + i\Gamma_1)} - \frac{\omega_{p2}^2}{\omega(\omega + i\Gamma_2)} \right). \tag{26}$$
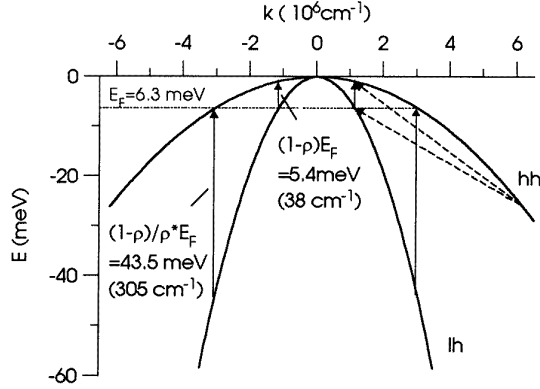
With $p_1/p_2 = (m_1/m_2)^{3/2}$, and for small relaxation times (or setting $\Gamma_1 = \Gamma_2$), an 'effective' plasma frequency

$$\omega_p^* = \sqrt{\frac{p}{\varepsilon_0 \varepsilon_\infty m^*}} \tag{27}$$

with

$$m^* = m_1 \frac{1 + \rho^{3/2}}{1 + \rho^{1/2}} \tag{28}$$

can be introduced, and the plasma behaves as if all of the carriers had the 'effective' mass m^* ($=0.43m_e$ in GaAs). In our example, $\omega_p^* = 140$ cm^{-1} is obtained. At this frequency

Figure 2. A schematic diagram of the band transitions at $T = 0$ K. For $q = 0$, only vertical interband transitions are allowed (solid lines); the range of energy transfer is noted for the case discussed in the text. For $q \neq 0$, diagonal transitions are possible, too. As examples, a hh $\rightarrow$ lh interband transition and a hh $\rightarrow$ hh intraband transition for $q = 5 \times 10^6$ cm^{-1} are drawn (dashed lines).

Re(ε) is zero, and the plasmon energy is given by the maximum of the spectral density Im($-1/\varepsilon$); see figure 1(a).
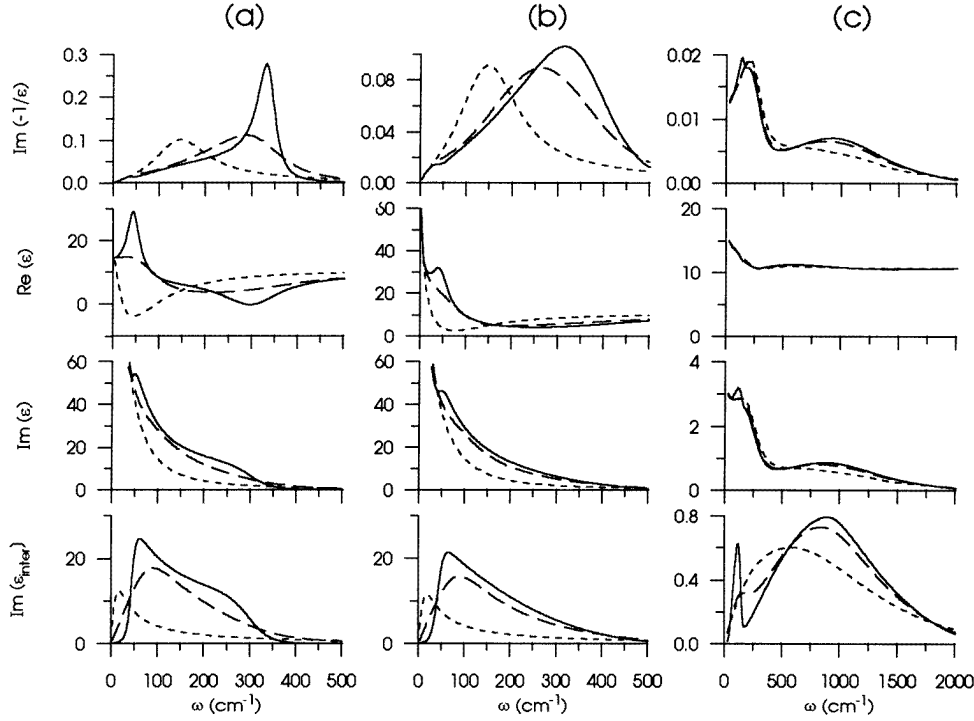
3.1.2. Low temperature; $\hbar\omega \gg kT$. The interband part gives a crucial contribution to the dielectric function, which can be simplified also by introducing an effective plasma frequency ω_p^{**}, with

$$m^{**} = m_1 \frac{2\rho}{1 + \rho}. \tag{29}$$

The plasma behaves as if all of the free carriers would move with the same 'effective' mass m^{**} (=$0.14m_e$ in GaAs), and the plasma frequency is shifted up. This case is demonstrated in figure 1(b), where $T = 1$ K was used in the calculations. In addition to Re(ε), Im(ε), and Im($-1/\varepsilon$) for the complete dielectric function, the imaginary part of ε_{inter} is shown, which is dominant in the energy region 50 to 300 cm^{-1}. Im($-1/\varepsilon_{inter}$) reflects the interband transitions between the bands of light and heavy holes, as can be seen in the schematic band model in figure 2. At $T = 0$ K, the bands of the heavy and light holes are filled up to the Fermi energy $E_F = 6.3$ meV. Since $q = 0$, only vertical transitions are allowed; their energy range is restricted to values between about $(1 - \rho)E_F = 5.4$ meV $\simeq 38$ cm^{-1} and $[(1 - \rho)/\rho]E_F = 43.5$ meV $\simeq 305$ cm^{-1}.

3.2. Temperature dependence

The mobility of the free holes is usually low in comparison with that of the free electrons. Therefore, we use in the following discussion the more realistic values of $\Gamma_1 = \Gamma_2 = 100$ cm^{-1} for the free-carrier dampings. In order to demonstrate the influence of finite-lifetime effects in the interband part, the three cases where $\Gamma_{12} = \Gamma_{21} \ll \Gamma_1 = \Gamma_2$ (the solid lines in figures 3 and 4), $\Gamma_{12} = \Gamma_{21} = \Gamma_1 = \Gamma_2$ (the dashed lines), and $\Gamma_{12} = \Gamma_{21} \gg \Gamma_1 = \Gamma_2$ (the dotted lines) are assumed. In figures 3 and 4, the spectral density Im($-1/\varepsilon$), the real part Re(ε), the imaginary part Im(ε), and the imaginary part of the interband contribution Im(ε_{inter}) are shown for low temperature and room temperature, respectively. For $q = 0$

Figure 3. The dielectric function $\varepsilon(\omega)$ at low temperature ($T = 5$ K) for different wavevectors: (a) $q = 10^4$ cm^{-1}; (b) $q = 10^6$ cm^{-1}; and (c) $q = 5 \times 10^6$ cm^{-1}; and interband part dampings: $\Gamma_{12} = 1$ cm^{-1} (solid line); $\Gamma_{12} = 100$ cm^{-1} (dashed line); and $\Gamma_{12} = 1000$ cm^{-1} (dotted line). The intraband dampings used were $\Gamma_1 = \Gamma_2 = 100$ cm^{-1}.

and low temperatures, we can compare figure 1(b) with figure 3(a). The interband part dominates for $\Gamma_{12} = \Gamma_{21} \lesssim \Gamma_1 = \Gamma_2$, and the spectral density and the effective plasma frequency are shifted to lower values with increasing interband damping, which shifts the imaginary part to lower energies. At room temperature (see figure 4), the intraband part dominates, and the effective plasma frequency is shifted closer to the ω_p^*-value. Due to the Fermi distribution, at this temperature, the free holes extend over many states, allowing transitions with higher energies; the imaginary part Im(ε_{inter}) extends to higher frequencies, its maximum value being more than one order smaller, as in the case of $T = 5$ K (see figures 3(a) and 4(a)).

3.3. Wavevector dependence

With growing q, the shape of the spectral density function Im($-1/\varepsilon$) becomes more and more broadened. Wavevector conservation enables diagonal transitions to occur within and between the two hole bands. This is shown schematically in figure 2 for the two transitions hh $\rightarrow$ hh and hh $\rightarrow$ lh, with $q = 5 \times 10^5$ cm^{-1} wavevector transfer. The latter transitions become possible at $T = 0$ K for $q > q_{F1} - q_{F2}$, and give rise to the low-frequency maximum in the imaginary part of ε_{inter}, which can be seen for small carrier dampings in figure 3.

The second maximum at higher frequencies in Im(ε_{inter}) is mainly due to lh $\rightarrow$ hh
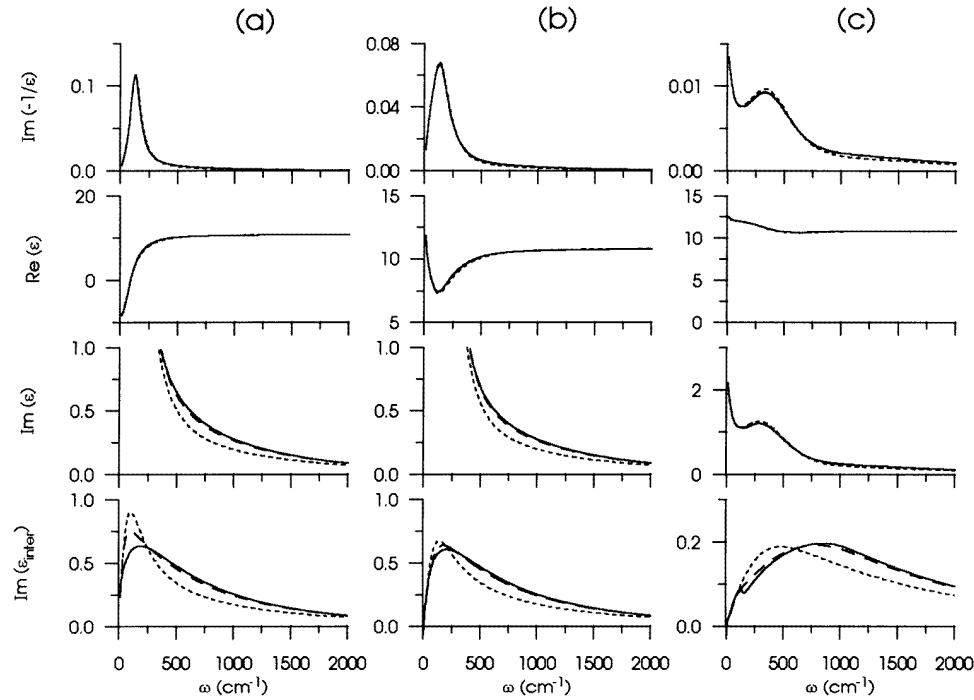
**Figure 4.** The dielectric function $\varepsilon(\omega)$ at room temperature ($T = 300$ K) for different wavevectors: (a) $q = 10^4$ cm^{-1}; (b) $q = 10^6$ cm^{-1}; and (c) $q = 5 \times 10^6$ cm^{-1}; and interband part dampings: $\Gamma_{12} = 1$ cm^{-1} (solid line); $\Gamma_{12} = 100$ cm^{-1} (dashed line); and $\Gamma_{12} = 1000$ cm^{-1} (dotted line). The intraband dampings used were $\Gamma_1 = \Gamma_2 = 100$ cm^{-1}.

transitions. With increasing temperature the maximum of $\mathrm{Im}(\varepsilon_{inter})$ is shifted to lower energies where $\mathrm{Im}(\varepsilon_{intra})$ dominates, and the shape of $\mathrm{Im}(-1/\varepsilon)$ is mainly determined by the intraband transitions (see figure 4).

For $q \neq 0$, in addition to the collective plasma excitations and interband transitions, transitions within the same bands are also allowed. The energy range of these single-particle excitations extends in a degenerate hole gas, at $T = 0$ K, and neglecting damping for $q = 10^6$ cm^{-1}, from zero up to 40 cm^{-1} (130 cm^{-1}) in the heavy (light) hole band. For $q = 5 \times 10^6$ cm^{-1}, the ranges of allowed transitions are 0 to 300 cm^{-1} (heavy holes), and 520 to 1400 cm^{-1} (light holes).

In figure 5 the regions of single-particle intraband excitations with $\mathrm{Im}(\varepsilon_{intra}) \neq 0$ are shown for heavy holes (between the solid lines) and light holes (between the chain lines) for $p = 10^{18}$ cm^{-3}, and $T = 0$ K, and neglecting carrier damping. The hatched region between the dashed lines corresponds to interband transitions. Because at $q \neq 0$ the shape of $\mathrm{Im}(\varepsilon_{inter})$ has no sharp contours, the hatched region was defined by $\mathrm{Im}(\varepsilon_{inter}) > (1/e)\,\mathrm{Im}(\varepsilon_{inter})_{max}$ at a given wavevector.

The collective plasma excitations are Landau damped if their energy reaches that of the single-particle excitations with increasing wavevector. However, in the case of the assumed limited carrier mobility, even at $T = 5$ K there is no sharply defined wavevector at which this process starts. The low-frequency tail of the band $\mathrm{Im}(-1/\varepsilon)$, which becomes more pronounced with increasing q (see figures 1 and 3), is due to intraband as well as interband single-particle excitations.
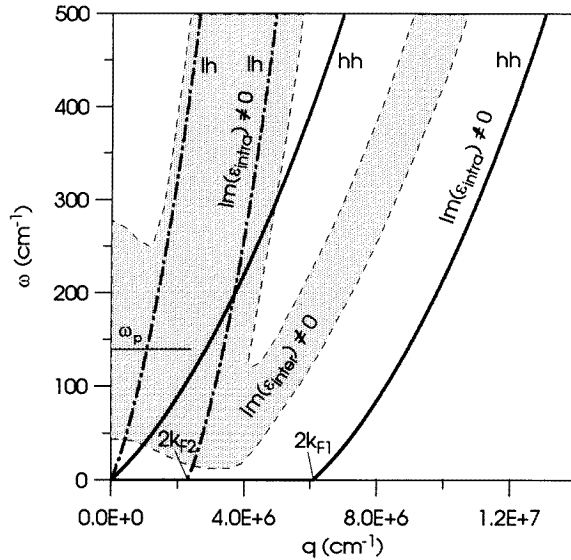
Figure 5. Single-particle excitations of the two-component plasma of heavy and light holes at $T = 0$ K. The continuum with $\mathrm{Im}(\varepsilon_{intra}) \neq 0$ between the solid lines is for the heavy holes, and that between the chain lines is for the light holes. The shaded area for interband transitions is defined by $\mathrm{Im}(\varepsilon_{inter}) > (1/e)\,\mathrm{Im}(\varepsilon_{inter})_{max}$ at a given wavevector. The frequency ω_p of the optic plasmon at $q = 0$ is marked by an arrow.

### 3.4. Comparison with light scattering experiments

Some features discussed earlier could be studied by means of light scattering experiments. Figure 6 shows Raman spectra of Zn-doped GaAs samples. An Ar$^+$-laser-pumped Ti:sapphire laser was used for excitation at $\lambda = 900$ nm, below the direct energy gap of GaAs ($E_g = 1.52$ eV at $T = 10$ K, which corresponds to $\lambda = 816$ nm). The spectra were taken in the backscattering configuration, with the laser beam perpendicular to the (100) surfaces of the single crystals. The signal was analysed with a triple monochromator, Jobin–Yvon T64000, and detected by a CCD multichannel detector.

A broad single-particle excitation spectrum is seen at low temperatures. The observed superimposed Fano-like structure in the frequency region of the optical phonons could be interpreted as an interference between the hole excitation continuum and the LO phonons [11], and will not be discussed here. The present discussion is concerned with the measured features of the single-particle continuum, in the framework of the dielectric function given above.

The maxima of the continuum are shifted to higher energies with increased free-hole concentrations, and correspond to vertical lh $\rightarrow$ hh interband transitions, which are shown schematically in figure 2. The wavevector transferred in the light scattering experiment is $q \approx 3 \times 10^5$ cm^{-1}.

A further proof that the observed single-particle spectrum is mainly due to interband transitions is obtained by measurements of the dependence on the temperature.

Figure 7(a) represents Raman spectra of a sample with the free-hole concentration $p = 8 \times 10^{18}$ cm^{-3} at 10 K and 300 K. A laser line at $\lambda = 951$ nm was used for the excitation, in order to avoid overlap of the room temperature Raman spectra with the
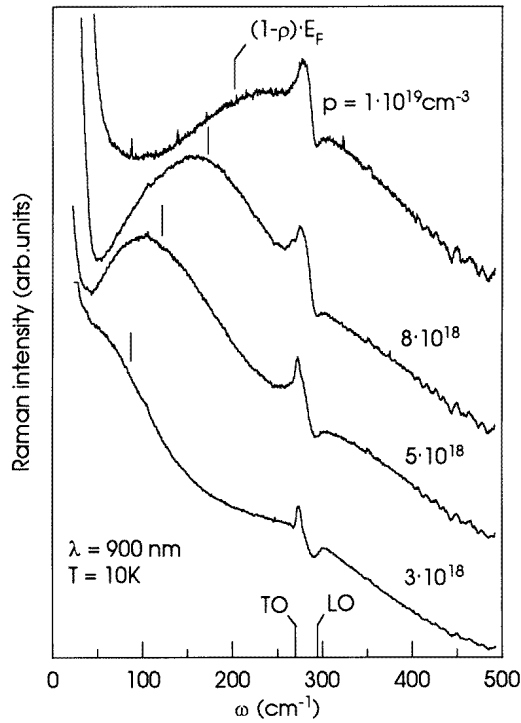
Figure 6. Raman spectra of p-type GaAs:Zn with laser excitation below the direct energy gap. In addition to the broad bands of single-particle excitations, a Fano-like interference in the region of the coupled LO-phonon–plasmon modes is observed.

luminescence.

In figure 7(b) the measurements are compared with calculations. The cross section of the light scattering spectrum can be written as

$$\frac{\mathrm{d}^2\sigma}{\mathrm{d}\omega\,\mathrm{d}\Omega} \sim (1 - \mathrm{e}^{-\hbar\omega/kT})^{-1} \operatorname{Im}\chi(\omega, k)$$

where $\chi(\omega, k)$ is a response function of the holes [12]. Because the periodic parts of the Bloch functions of different bands are orthogonal to each other, the interband transitions are not accompanied by charge-density fluctuations as they are in the case of intraband ones. Therefore, they are not screened, and are seen in the light scattering spectra. The dotted lines in figure 7(b) show $\operatorname{Im}\chi_{inter}$ for $T = 10$ K and room temperature. The solid lines take into consideration the Bose factor and intraband parts. The damping parameters $\Gamma_1 = 230$ cm^{-1} and $\Gamma_2 = 610$ cm^{-1} were deduced from the measured Hall mobility $\mu_H = 90$ cm^2 V^{-1} s^{-1}, where hole scattering by ionized impurities was assumed to be the dominant scattering process. Γ_{12} was taken to be the mean value of the mobilities in the two bands. The dependence on temperature of the theoretical curves corresponds well with the experimental results, but the correspondence could be improved by taking into consideration the fact that the spectral sensitivity of the CCD detector decreases with larger Stokes shifts in the near-infrared region.
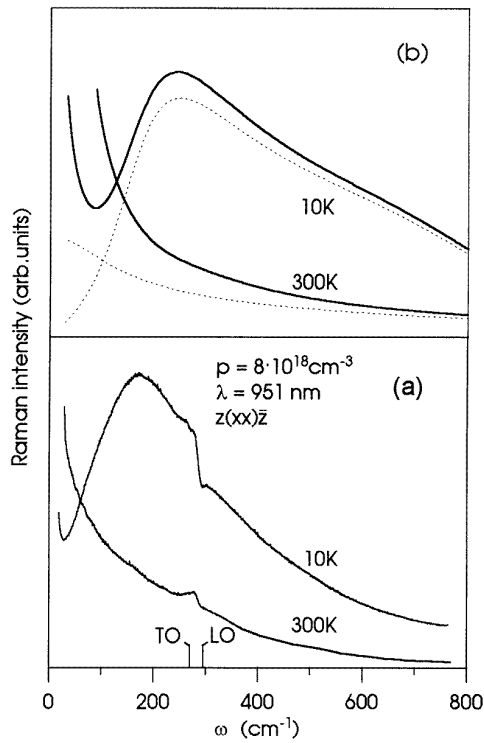
Figure 7. A comparison between the measured (a) and calculated (b) Raman scattering intensity for a GaAs:Zn sample, with $p = 8 \times 10^{18}$ cm^{-3} at low (10 K) and at room temperature (300 K). Contributions due to the interband part of the dielectric function are indicated by dashed lines in (b).

4. Conclusion

In summary, the dependences on frequency, wavevector, and temperature of the low-frequency dielectric functions of p-type semiconductors have been studied. The random-phase approximation was used, and finite-lifetime effects for the holes were included in a generalized Mermin approximation.

Using parameters characteristic of p-GaAs, it was shown that, at low temperatures and small wavevectors, interband transitions give important contributions to the dielectric function, even under conditions of low hole mobility. The calculations were compared with light scattering experiments on Zn-doped GaAs.

Acknowledgment

References

[1] Combescot M and Nozières P 1972 *Solid State Commun.* **10** 301
[2] Combescot M and Nozières P 1972 *J. Phys. C: Solid State Phys.* **5** 2369
[3] Bardyszewski W 1986 *Solid State Commun.* **57** 873

[4] Monecke J 1984 *Phys. Status Solidi* b **121** 329
[5] Mermin N D 1970 *Phys. Rev.* B **1** 2362
[6] Wiley J D 1975 *Semiconductors and Semimetals* vol 19, ed R K Willardson and A C Beer (New York: Academic) ch 2
[7] Dresselhaus G, Kip A F and Kittel C 1955 *Phys. Rev.* **98** 368
[8] Luttinger J M and Kohn W 1955 *Phys. Rev.* **97** 969
[9] Luttinger J M 1956 *Phys. Rev.* **102** 1030
[10] Kane E O 1956 *J. Phys. Chem. Solids* **1** 82
[11] Irmer G, Wenzel M and Monecke J 1996 *Proc. 23rd Int. Conf. on the Physics of Semiconductors (Berlin, 1996)* vol 1 (Singapore: World Scientific) p 217
[12] Abstreiter G, Cardona M and Pinczuk A 1984 *Light Scattering in Solids IV* ed M Cardona and G Güntherodt (Berlin: Springer) p 5